1D System Modeling and 3D CFD Co-Simulation Methodology for Analyzing Transient Behavior in Hydraulic Valves

Priyanka Viswanath[1,*], Nathan Rosenbaum[2], Chris Imholte[2], Ashutosh Pandey[1] and Bipin Kashid[2]

[1]*Simerics Inc.*

[2]*Parker-Hannifin*

[*]*corresponding author: pv@simerics.com*

Abstract.

Hydraulic valves are key components in fluid power systems and are required to operate reliably over wide pressure, flow, and temperature ranges, often under fast-changing load conditions. As hydraulic systems become more compact, complex interactions between valves and the surrounding sub-system can lead to undesirable phenomena such as noise and dynamic instabilities. These effects can degrade system performance, damage components, and negatively impact operator experience. Identifying the root cause of such behavior is challenging and frequently relies on repeated prototyping and extended testing, increasing development time and delaying product launch. This paper presents a decoupled co-simulation methodology for modeling transient flow behavior and instabilities in hydraulic valves. The approach combines one-dimensional (1D) sub-system modeling with three-dimensional (3D) Computational Fluid Dynamics (CFD) analysis using Simerics-MP+. The 1D models establish the operating envelope and are validated against test data to define the boundary conditions for high-fidelity 3D CFD simulations. Targeted CFD analysis enables the identification of operational deviations, cavitation, jets, flow separation and ensuing vortices, which are critical in identifying local instabilities. These detailed insights are difficult to obtain through 1D analysis or to capture experimentally. By maintaining a decoupled framework, the methodology ensures computational efficiency while preserving realistic system behavior. The results demonstrate reduced prototyping cycles and accelerated valve development, providing a practical and scalable approach for resolving complex dynamic issues in modern hydraulic valve designs.

Keywords. Hydraulic valves, CFD, 1D system modeling, valve dynamics, transient flow behavior, instabilities, cavitation.

1. INTRODUCTION

Fluid power systems rely on hydraulic valves to precisely regulate pressure and flow under demanding and rapidly varying operating conditions. As system architectures become more compact and performance requirements more stringent, valve dynamics become increasingly sensitive to interactions with the surrounding circuit. These interactions can manifest as oscillations, cavitation, and flow-induced instabilities that compromise reliability and operator comfort. In hydraulic components, cavitation in particular can lead to vibrations, pressure pulsations, noise, and surface erosion [1], while unsteady flow through valve passages generates pressure fluctuations that propagate as structural excitation throughout the system [2]. Computational Fluid Dynamics (CFD) analysis has been applied to characterize internal flow behavior in various hydraulic valve types, including pressure control valves [3], directional control valves constructed from logic elements [4], flow force reduction in hydraulic valves [5], and noise mitigation in relief valves using hybrid CFD-acoustic approaches [6]. Despite these advances, diagnosing transient instabilities and failure modes under realistic system boundary conditions remains challenging, and development programs frequently address them through iterative build-and-test cycles that are both time-consuming and costly.

Simulation has become an indispensable tool in hydraulic valve development. Lumped parameter models in which valve flow passages are represented as orifices, volumes, and springs are widely used for system-level analysis owing to their low computational cost [1]. However, the simplifying assumptions inherent to this approach limit its ability to resolve spatially distributed phenomena such as localized pressure gradients, jet formation, flow separation, cavitation and instabilities. Gasche et al. [7] demonstrated this directly in the context of compressor suction valves, showing that while a one-dimensional (1D) model predicts global force and displacement well, it cannot capture local flow detail essential for design refinement. Three-dimensional (3D) CFD analysis resolves these effects with high fidelity and can reveal internal flow patterns that are difficult or impossible to obtain experimentally [2]. Dynamic valve simulations using moving mesh approaches and coupled valve motion models have been demonstrated using the commercial CFD code Simerics-MP+ in related applications [8, 9], establishing the solver's capability for transient valve-fluid interaction problems. However, applying three-dimensional CFD indiscriminately across a full operating envelope is computationally prohibitive, and coupled 1D–3D frameworks have been proposed across a range of hydraulic system applications to address this [10, 11]. Most recently, Schmid et al. [12] demonstrated a directly analogous methodology for pressure relief valves in a hydropower system, where 1D model calibration revealed irregular discharge characteristics that could not be explained at the system level, and targeted 3D CFD analysis identified cavitation and geometric flow restrictions as the governing mechanisms; findings that were subsequently used to refine the 1D model. The application of such decoupled multi-scale approaches to industrial hydraulic valves under transient operating conditions, including failure mode diagnosis and design iterations, remains an active area of development.

This paper presents such a methodology, applied to two poppet-style hydraulic valves developed by Parker-Hannifin: a Poppet-style Logic Element (PLE) and an Electro-Proportional Flow (EPF) control valve. System-level 1D models first characterize normal operation and establish validated boundary conditions. 3D CFD in Simerics-MP+ then targets the cases where system-level analysis falls short. Both valves were identified as exhibiting dynamic behavior that could not be adequately explained or reproduced through 1D system modeling alone. For the PLE, high-frequency poppet oscillations observed experimentally at low flow rates under elevated spring loads are investigated. For the EPF, a pressure-dependent failure mode is diagnosed through analysis of the internal pressure zones, leading to a targeted design modification that is validated in simulation and subsequently confirmed through physical testing. Together, the two case studies demonstrate how the decoupled 1D–3D framework can be used to simulate realistic valve behavior, thereby accelerating design iterations, and reducing prototyping cycles in the development of modern hydraulic valves.

2. MODELS

Two hydraulic valves developed by Parker-Hannifin are considered in this study: a Poppet-style Logic Element (PLE) and an Electro-Proportional Flow (EPF) control valve. The PLE is a 2-way pilot-operated cartridge valve designed for directional flow control of hydraulic systems at flows and pressures that exceed the limits of conventional cartridge valves. A cross-sectional view is shown in Figure 1a, where port 3 is the pilot port. When piloted by low-flow control elements, the PLE act as a high-capacity switch, allowing a wide variety of flow path changes analogous to multi-way spool valves, while preventing inter-port leakage that a spool would otherwise allow. The PLE has a 2:1 pilot ratio such that the area on which the pressure acts in the pilot chamber is twice that of the port 1 seat area and the port 2 differential area between the seal and the seat. Since the areas at ports 1 and 2 are equal, the valve is biased closed by a spring in the pilot chamber and opens only when the pressure at either port 1 or port 2 exceeds the load of the bias spring.

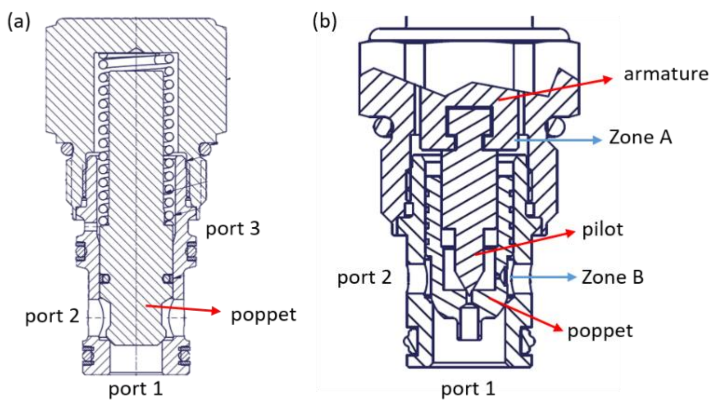

Figure 1: Cross-section views of the valve models. (a) Poppet-style Logic Element (PLE), with port 3 as the pilot port. (b) Electro-Proportional Flow (EPF) control valve, showing the pilot, poppet, and key zones.

The EPF is a poppet-style normally closed electro-proportional flow control valve used in load-holding applications to control flow into or out of a cylinder, while blocking leakage that would allow loads to drift when the valve is not engaged. This dual function simplifies hydraulic circuits by combining the functions of a spool valve for directing flow and a check valve for preventing leakage. A cross-sectional view is shown in Figure 1b. In the de-energized state, the internal springs hold the pilot against the poppet and the poppet against an internal seat, sealing the flow path from port 2 to port 1. Pressure builds behind the poppet (Zone A), adding to this closing force. When the solenoid is energized, the pilot lifts from the poppet allowing the pressure in Zone A to vent to port 1. The resulting pressure at port 2, acting on the differential area between the poppet outer diameter and seat diameter (Zone B), overcomes the reduced closing force and lifts the poppet off the seat, allowing controlled flow from port 2 to port 1. When the solenoid is de-energized, the pilot reseats against the poppet, and the combined action of the return spring and the recovering pressure in Zone A pushes the poppet back against the seat.

3. MODELING APPROACH

A co-simulation methodology is employed that combines 1D system modeling with 3D CFD analysis. The 1D models are developed first to capture system-level behavior and run across the full range of operating conditions, with certain assumptions refined iteratively. For edge cases and worst-case operating scenarios, 3D CFD provides higher-fidelity insight into local flow behavior, instabilities, extent of cavitation, jet formation, and operational deviations that are difficult to resolve with 1D models alone. The boundary conditions and parameters used to model the valve motion in the 3D CFD models are derived directly from the 1D results, ensuring that the CFD simulations reflect realistic system behavior while maintaining computational efficiency.

3.1. 1D

1D simulations are developed in Amesim, with some general assumptions made, including but not limited to:

- Physical parts do not include non-conformances.
- Certain flow passages are sufficiently non-restrictive as to act as one volume.
- Certain volumes are sufficiently restrictive as to be treated as an orifice rather than a volume.

Parameters relating to fluid inertia were left at the default values provided by Amesim. For the PLE, the seal friction, being a specialty seal, could be incorporated into the friction of the poppet mass, rather than as an independent pressure dependent model element. Key factors in achieving close agreement with real world valve performance include the selection of which flow passages are treated as volumes versus restrictive orifices, the inclusion of the cavity surrounding the cartridge in the manifold block in which the cartridge is installed, and the application of varying types of friction.

The EPF model includes two additional assumptions:

- The solenoid function operates normally, and as such, its behavior could be assumed as a direct force input, rather than considering how its components influence the conversion of electrical power to the physical force acting on the moving components of the valve.
- The nature of the link between the pilot and solenoid armature is such that the two components could be considered as one mass.

3.2. 3D CFD

3.2.1. Governing Equations

3D CFD simulations are performed in Simerics-MP+. The integral form of the unsteady conservation of mass and momentum equations is solved [13].

Cavitation is modeled using Constant Gas Mass Fraction model available in Simerics-MP+, which accounts for both liquid-vapor phase change and the presence of non-condensable gases. In this model, the mass fraction of non-condensable gases is held constant and is treated as an ideal gas [13, 14].

Valve motion is modeled using a translational one-degree-of-freedom (1-DOF) formulation, applied either as a prescribed position or a force balance. In the prescribed position approach, valve displacement is specified as a user-defined function of time. In the force balance approach, the valve position is determined by solving a scalar linear momentum equation:

$$m\frac{d^2s}{dt^2} = F_{hydrodynamic} - F_{damping} - F_{spring} \tag{1}$$

where m is the mass of the solid body and s is the magnitude of the solid body's position vector. The hydrodynamic force comprises pressure and shear contributions from the relative motion between the fluid flow and the surfaces of the solid body which are in contact with the flow:

$$F_{hydrodynamic} = \sum F_{pressure} + \sum F_{shear} \tag{2}$$

The damping force is a retarding force proportional to the velocity determined by the motion of the solid body and a user-specified damping coefficient D:

$$F_{damping} = D\frac{ds}{dt} \tag{3}$$

The spring force depends on the spring preload $F_{preload}$, spring constant k, and displacement of the spring, d:

$$F_{spring} = F_{preload} + kd \tag{4}$$

3.2.2. Simulation Setup

Hydraulic oil properties are used for all simulations. The setup differs between the two valves, reflecting differences in their operating modes and internal complexity. All results and boundary conditions are presented in normalized form to protect proprietary design information while preserving the underlying flow physics.

For the PLE, two operating conditions are considered: flow from port 1 to port 2 (OP1) and flow from port 2 to port 1 (OP2). A volumetric flux inflow boundary condition is applied at the inlet, ramped from 0 to 1 unit and back to 0 unit. The outlet has a specified pressure boundary condition at atmospheric pressure. Although physical test ramps span 30–60 seconds, CFD ramps are performed over 1 second with a time step of approximately 0.15 millisecond. Sensitivity studies confirmed that the shorter ramp duration produces equivalent results, significantly reducing computational cost. The time step size used ensures a minimum of 100 time steps per cycle, where the cycle frequency corresponds to the natural frequency of the valve body. This resolution aligns with established best practices for accurately capturing valve dynamics. Poppet motion is modeled using a single 1-DOF force balance model, with poppet mass, spring constant, preload, and damping coefficient specified as user inputs. A closure model is applied to handle complete valve seating, without having to compress the corresponding mesh volumes to zero. The flow in the cells between the valve body and valve seat is cut off when gap between them is below a certain specified value. In the PLE, this gap is set to 25 µm. The pilot port and chamber are excluded from the PLE model, as the case simulated represents a worst-case scenario in which no pilot pressure signal is applied. In this condition, the large opening at port 3 allows oil to escape freely as the poppet lifts, rendering pilot chamber damping negligible.

Flow in the EPF is from port 2 to port 1, with pressure boundary conditions specified both at the inlet and the outlet. Three inlet pressures are simulated namely P_{low}, $P_{intermediate}$ and P_{high}, with the outlet set to atmospheric pressure. Three translation 1-DOF models are used for the three bodies that can move independently. The pilot and armature are modeled with a prescribed displacement ramped linearly over time. They are treated as a single combined mass consistent with the 1D model. The poppet motion is governed by a force-balance, with its position bounded by the pilot position. Closure models are applied to both the poppet and pilot, with a gap limit of 100 µm. A time step of approximately 0.05 millisecond is used.

4. MESH

Simerics-MP+ uses a binary-tree meshing algorithm to create a mesh comprising primarily hexahedral elements, with tetrahedral elements used where hexahedral elements cannot adequately resolve local geometry, primarily on the surface of the volumes. Additionally, a deforming mesh strategy is used to model the motion of the valves, which preserves mesh topology throughout the simulation, eliminating the need for remeshing. This ensures solution continuity without facing interpolation errors and removing the computational overhead associated with dynamic mesh refinement. The stationary and deforming fluid volumes are meshed separately. The deforming volumes are meshed using the Valve Template offered in Simerics-MP+, which automatically assigns boundary conditions and optimizes the mesh to accommodate both deformation and valve closure.

Cross-sectional views of the mesh for each valve are shown in Figure 2. The PLE mesh comprises approximately 450,000 cells (Figure 2a), and the EPF mesh approximately 922,000 cells (Figure 2c). A mesh independence study was conducted using a finer grid resolution, which exhibited negligible differences in results. Hence, these baseline mesh densities were used for computational efficiency. The mesh can be compressed to a gap of a few microns to represent the physically closed valve position, as shown for the PLE in Figure 2b and the EPF in Figure 2d. In the EPF, the leakage gap between the poppet and the cage is meshed using the Annulus Template, which generates a high quality orthogonal mesh in gaps on the order of microns. The motion of the valve is dictated by the translation 1-DOF model calculations. Flow communication between separate meshed volumes is handled using Mismatched Grid Interfaces (MGIs) in Simerics-MP+, which allow flux to pass through a shared interface between volumes regardless of node alignment. The interface can be created between stationary or moving boundaries. For moving boundaries, it is automatically recalculated at each time step.

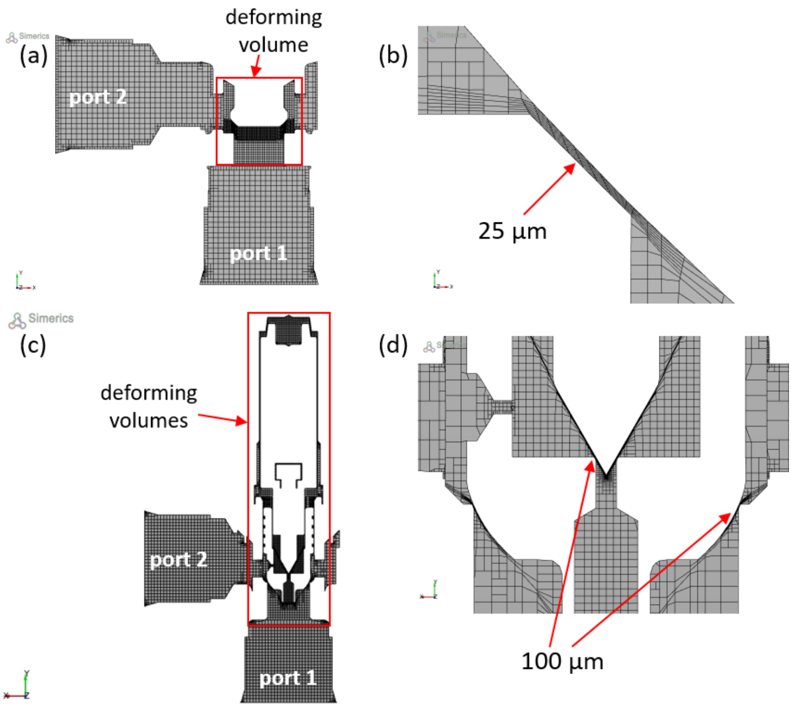

Figure 2. Mesh resolution in the PLE and EPF. (a) Cross-sectional view of the PLE mesh. (b) Close-up of the PLE mesh where the poppet physically touches the valve seat, showing a mesh compressed into a 25 µm gap. (c) Cross-sectional view of the EPF mesh. (d) Close-up of the mesh where the poppet physically touches the valve seat and the pilot touches the poppet, showing a mesh compressed into in a 100 µm gap.

The EPF presents an additional meshing consideration due to the three independently moving valve bodies. The pilot and armature travel together under electromagnetic actuation while the poppet moves separately due to hydraulic forces. As the travel distances and dynamics of these bodies are independent, their mesh deformations are handled separately, which is handled by the meshing capabilities of Simerics-MP+.

5. RESULTS AND DISCUSSION

5.1. PLE

In testing, the PLE exhibits unstable behavior at higher bias spring loads. With no pilot pressure applied, as the flow increases from either port 1 or 2, the poppet oscillates at high frequency until the flow rate is sufficient to push the poppet fully against its stop. A similar instability recurs as flow decreases and the poppet returns toward the seat. 3D simulation was employed to gain greater insight into how fluid behavior could influence the lift forces acting on the poppet, with the objective of identifying potential poppet designs that maximize lift force to overcome the opposing hydrodynamic forces resisting valve opening. The following results are presented in normalized form as:

$$\theta^* = \frac{\theta}{\theta_{ref}} \tag{5}$$

Where, θ is any physical quantity and θ_{ref} is a reference or maximum value of that quantity.

The simulation results are validated against test data. Figure 3a shows pressure drop versus flow rate for operating condition OP1, with the volumetric flux ramped from 0-1 unit and back to 0 unit. Figure 3b shows the corresponding data for operating condition OP2. The region of instability observed in tests at low flow rates is captured in the 3D CFD results for both OP1 and OP2, though the predicted oscillation amplitudes are higher than measured. The amplitude can be tuned by adjusting the damping coefficient. however, the objective of this study was to capture the extent of the instability region rather than its amplitude, and the current inputs are appropriate for that purpose. Once the instabilities subside, both the test and CFD results show a similar pressure drop between the 0-1 and 1-0 unit ramps. Figure 3c shows the 1D simulation results, in which both stiction and coulomb friction are included. The 1D model also captures the instability region, though the oscillations decay at a lower flow rate.

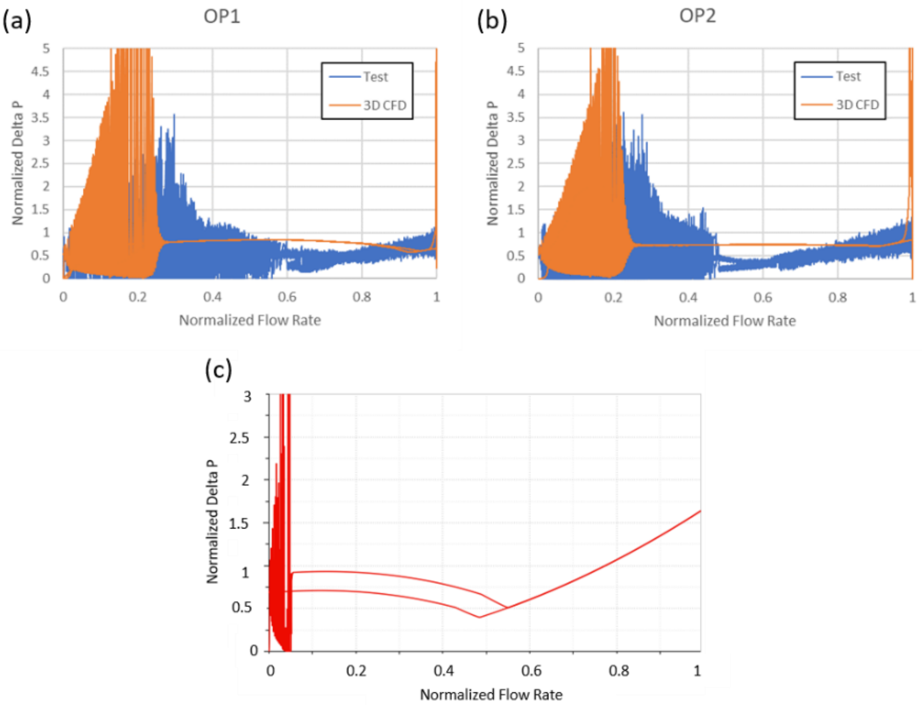

Figure 3: Validation against test data. (a) Test and 3D CFD data showing the pressure drop over flow rate for operating condition OP1. (b) Test and 3D CFD data showing the pressure drop over flow rate for operating condition OP2. (c) 1D simulation showing the instabilities in pressure drop in the low flow rate region.

Figures 4a and 4b show valve lift versus flow rate for OP1 and OP2 respectively, with each plot showing both the 0-1 as well as 1-0 unit ramps. The oscillations in displacement are lower during the decreasing ramp from 1-0 unit, in both OP1 and OP2. Once the oscillations die down, the lift profiles converge closely until the poppet begins to bottom out, where minor differences are observed. The poppet reaches its travel stop at flow rates above approximately 0.9 unit in both conditions. While the overall behavior in OP1 and OP2 is similar, displacement oscillations during the 0-1 unit ramp are marginally higher in OP1.

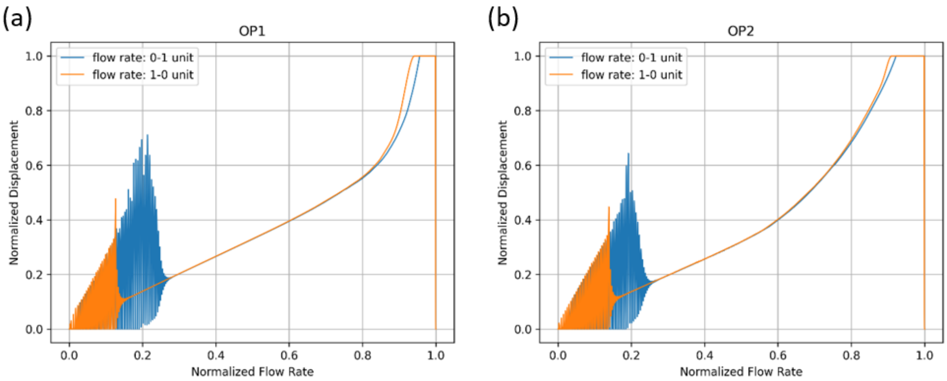

Figure 4: Valve lift versus flow rate. 3D CFD data showing the poppet lift versus flow rate with both the ramp up from 0-1 unit as well as the ramp down from 1-0 unit (a) for OP1, (b) for OP2.

Figures 5a and 5b show the hydrodynamic force acting on the poppet as a function of flow rate, for OP1 and OP2 respectively. The variation in fluid force is larger during the increasing ramp from 0-1 unit in both OP1 and OP2, with peak values of approximately 1 unit, nearly double those observed during the decreasing ramp from 1-0 unit. Once the oscillations subside, the hydrodynamic force is consistent in both the increasing and decreasing ramps. The valve instability is triggered at lower flow rates, which corresponds to low valve lift positions where pressure drop is highest. During the flow rate ramp up from 0-1 unit, the accelerating fluid could increase the kinetic energy imparted to the system, providing negative damping that could induce high amplitude oscillations that also take longer to dissipate. Conversely, when the flow rate is ramped down from 1-0 unit, the decelerating fluid could provide positive hydrodynamic damping, which suppresses oscillation amplitudes and delays the onset of instability. This delay could further be aided by the inertia of the fluid and the momentum of the moving poppet. Differences between OP1 and OP2 are pronounced in the oscillatory region, with slightly higher fluid forces in OP1 during the ramp up from 0-1 unit.

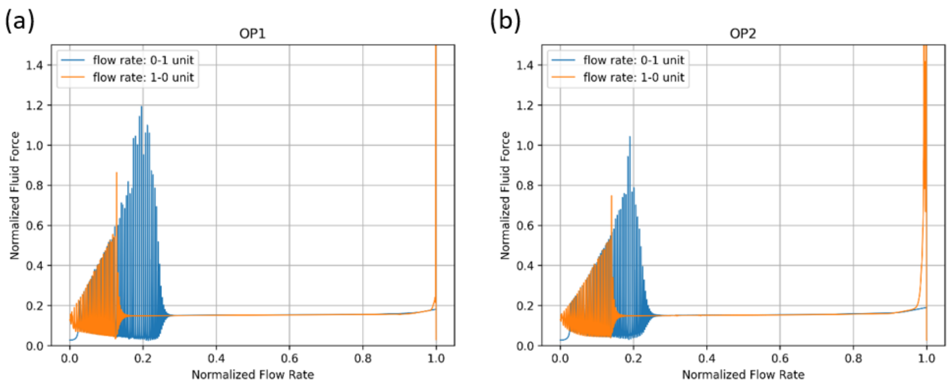

Figure 5: Hydrodynamic force versus flow rate. 3D CFD data showing the hydrodynamic force acting on the valve versus flow rate with both the ramp up from 0-1 unit as well as the ramp down from 1-0 unit (a) for OP1, (b) for OP2.

Examination of the pressure contours shows that the inlet port becomes pressurized up to a threshold level, above which poppet oscillations subside and stable lift begins. Figures 6a and 6c show this condition for operating conditions OP1 and OP2 respectively. As flow rate continues to increase toward 1 unit, the inlet port progressively depressurizes, as seen in Figures 6b and 6d at maximum flow. In condition OP2, where the poppet reaches its stop at a slightly lower flow rate than in OP1, pressure builds again at the inlet port once the poppet is fully bottomed-out, which is apparent in Figure 6d when compared to Figure 6b at the same flow rate.

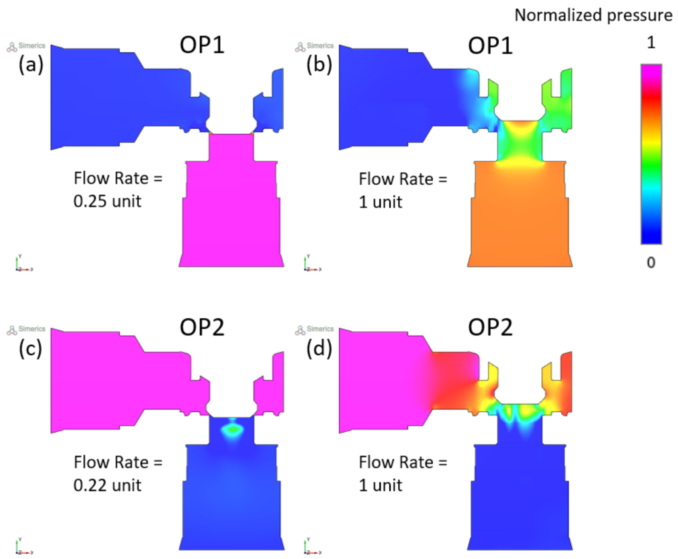

Figure 6: Cross-section showing the pressure contours in the PLE. (a) OP1 at the onset of stable lift. (b) OP1 when the poppet has bottomed-out and the flow rate reaches 1 unit. (c) OP2 at the onset of stable lift. (d) OP2 when the valve has bottomed-out and the flow rate reaches 1 unit.

Velocity contours at the same flow rate conditions are shown in Figure 7. Figure 7a shows operating condition OP1, where flow enters the narrow gap between the poppet and valve seat at a high velocity as the poppet begins stable lift, eventually forming a jet reaching 0.4-0.6 unit at the maximum flow rate of 1 unit, as seen in Figure 7b. A stagnation point is visible on the poppet face at port 1 in Figure 7b. Operating condition OP2 is depicted in Figure 7c, where the jet forms directed toward the outlet port, reaching a peak core velocity of approximately 1 unit at a flow rate of 1 unit. A stagnation point at a similar location on the poppet face is observed in OP2, as the jet exits through port 1.

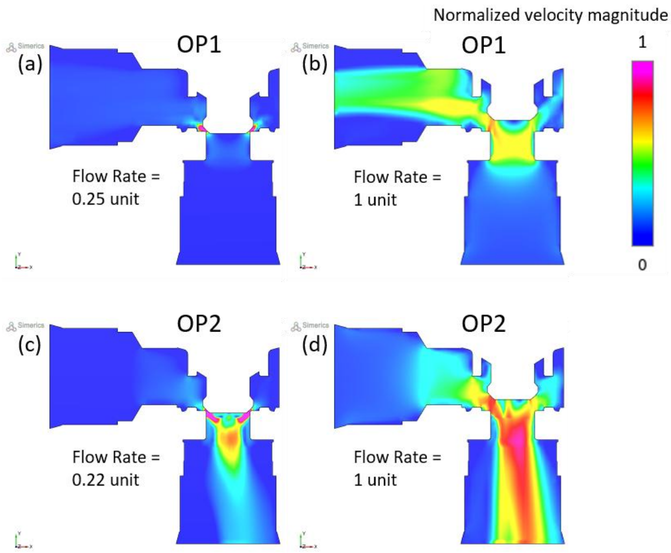

Figure 7: Cross-section showing the velocity contours in the PLE. (a) OP1 at the onset of stable lift. (b) OP1 when the poppet has bottomed-out and the flow rate reaches 1 unit. (c) OP2 at the onset of stable lift. (d) OP2 when the valve has bottomed-out and the flow rate reaches 1 unit.

Cavitation is quantified by the average volume fraction of the total gas, which accounts for vapor, dissolved gas, and free non-condensable gas phases combined. Figure 8 shows isosurfaces of regions where the total gas volume fraction exceeds 0.1, colored by volume fraction magnitude. Figure 8a shows cavitation bubbles in operating condition OP1 which first appears around the poppet–seat interface as the valve begins to open. The largest cavitation region occurs when the maximum flow rate of 1 unit is reached, as seen in Figure 8b, extending into the outlet port 2. The highest volume fraction of gas is concentrated near the entrance to port 2. In OP2, the initial cavitation bubble forms in a similar location, as seen in Figure 8c, and also reaches its maximum extent at 1 unit where it extends into the outlet port 1, as show in in Figure 8d. The cavitation bubble in OP2 extends into port 1 at maximum flow, with the highest gas fraction concentrated near the poppet face. The differences in cavitation extent and distribution between OP1 and OP2 reflect the distinct flow paths and jet orientations characteristic of each operating condition.

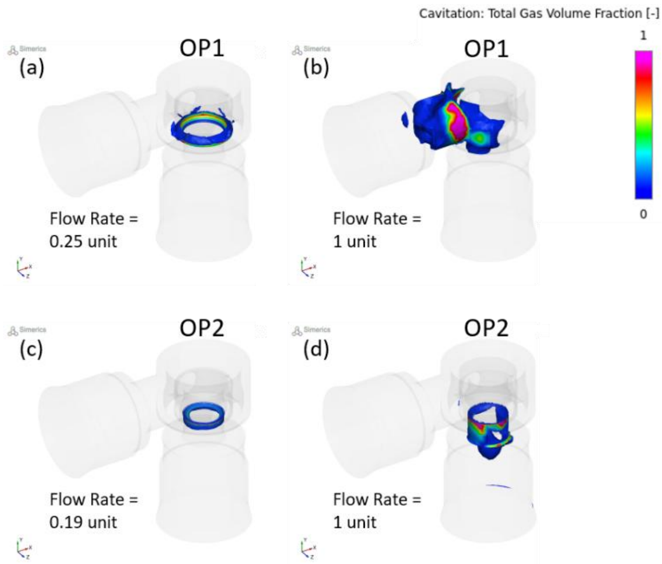

Figure 8: Regions where total gas volume fraction > 0.1 in the PLE. (a) OP1 at the onset of stable lift. (b) OP1 when the poppet has bottomed-out and the flow rate reaches 1 unit. (c) OP2 at the onset of stable lift. (d) OP2 when the valve has bottomed-out and the flow rate reaches 1 unit.

This methodology is being applied to evaluate multiple design variations of the poppet, with the objective of reducing instability at low flow rates. Key metrics include the hydrodynamic force acting on the poppet and the evolution of pressure and velocity fields as the poppet lifts and seats across a range of flow rates. Together, these diagnostics enable rapid screening of poppet design variants, identifying promising designs and eliminating underperforming ones based on computed lift force, pressure, and velocity fields, before any physical prototype is committed to manufacture or test.

5.2. EPF

In early testing, the valve did not perform as expected, failing to open above certain inlet pressures. Test data indicated that the solenoid was successfully lifting the pilot, but the poppet was not lifting off the seat. Several 1D models were developed that reasonably represented the expected behavior of the valve, but this particular failure mode could not be replicated. A 3D CFD model was developed to resolve fluid effects not captured by the 1D analysis. The CFD model reproduced the pressure dependency of the performance, revealing that above a certain inlet pressure, the pressure in Zone A does not drop sufficiently for the poppet to lift. A specific feature was found to control this behavior, and was proposed as a design change. The original design is referred to as Design 1 and the new proposed design as Design 2 in the results that follow. Similar to the PLE, the results are presented in a normalized form.

Figure 9 shows the displacement of the armature and the poppet at different inlet pressures for both Design 1 and Design 2. The armature displacement is identical across both designs. In Design 1, the poppet lifts at P_{low} but fails to lift at $P_{intermediate}$. In Design 2, the poppet lifts successfully at $P_{intermediate}$, closely tracking the armature and pilot displacement. A lag between armature lift and poppet response is also visible in Design 1 at P_{low}, which is negligible in Design 2.

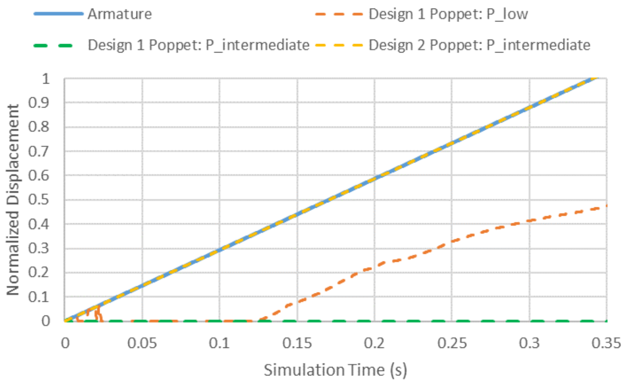

Figure 9: Valve Lift. Simulation data showing the valve lift for the armature and the poppet at different inlet pressures in both Design 1 and Design 2.

Figure 10 shows pressure contours in the EPF at key operating conditions. Figure 10a shows the pressure contours in Design 1 at an inlet pressure of P_{low}. The pressure drop in Zone A in this case is sufficient to allow the poppet to open. At $P_{intermediate}$, however, the poppet remains seated even as the pilot lifts, which can be observed in Figure 10b, indicating that the pressure in Zone A does not drop low enough to overcome the closing force. Figure 10c shows Design 2 at $P_{intermediate}$, where the pressure in Zone A is substantially lower than in Design 1 at the same condition, enabling the poppet to lift. The proposed design modification successfully resolved the operational deviation, and simulations confirmed that the poppet in Design 2 lifts reliably at inlet pressures up to P_{high}.

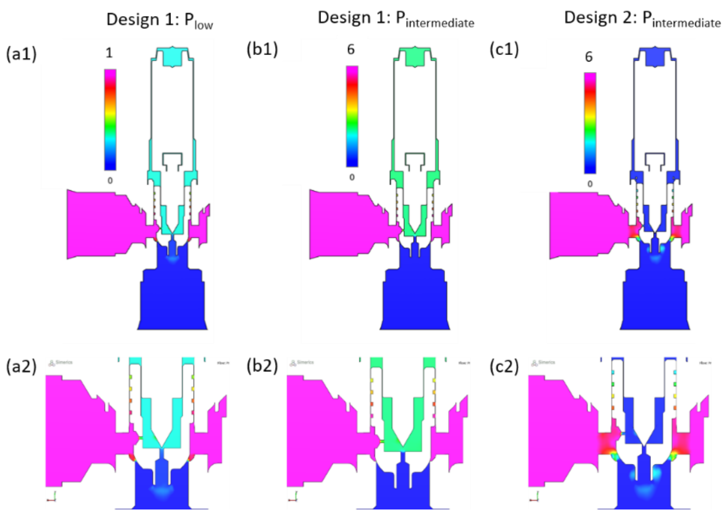

Figure 10: Cross-section showing the pressure contours in the EPF. (a1) Design 1 at inlet pressure P_{low}, where the poppet lifts successfully. (a2) Detailed view of the poppet and pilot lift region for Design 1 at P_{low}. (b1) Design 1 at inlet pressure $P_{intermediate}$, where the poppet fails to lift. (b2) Detailed view of the poppet and pilot lift region for Design 1 at $P_{intermediate}$. (c1) Design 2 at inlet

pressure $P_{intermediate}$, where the poppet lifts successfully. (c2) Detailed view of the poppet and pilot lift region for Design 2 at $P_{intermediate}$

Figure 11 shows pressure histories at three probe locations for both designs at an inlet pressure of $P_{intermediate}$. As the pilot and armature begin to lift, the pressure drop across these regions is approximately 0.4 unit greater in Design 2 than in Design 1, providing the additional pressure differential needed for the poppet to overcome the opposing spring forces and lift. The pressure drop in Design 1 is also more gradual, further reducing the available opening force.

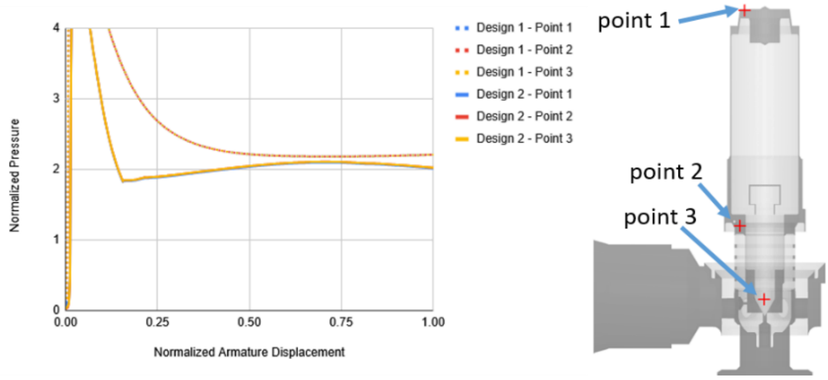

Figure 11: Pressure at probe locations. Pressure is monitored at three probe points placed in key regions in the EPF over increasing armature displacement, showing a higher pressure in Design 1 compared to Design 2.

Figure 12 shows the velocity contours in the EPF. Figure 12a shows the formation of a jet in Design 1 as the poppet lifts at an inlet pressure of P_{low}, with a core velocity of approximately 0.43 unit. At an inlet pressure of $P_{intermediate}$, though the poppet does not lift, there is some flow from port 2 to port 1 through orifices in the poppet as seen in Figure 12b. The design change in Design 2 allows the poppet to lift at $P_{intermediate}$, with Figure 12c showing the formation of a jet with a core velocity of about 2.14 unit as the poppet lifts, consistent with the significantly higher operating pressure compared to the P_{low} condition.

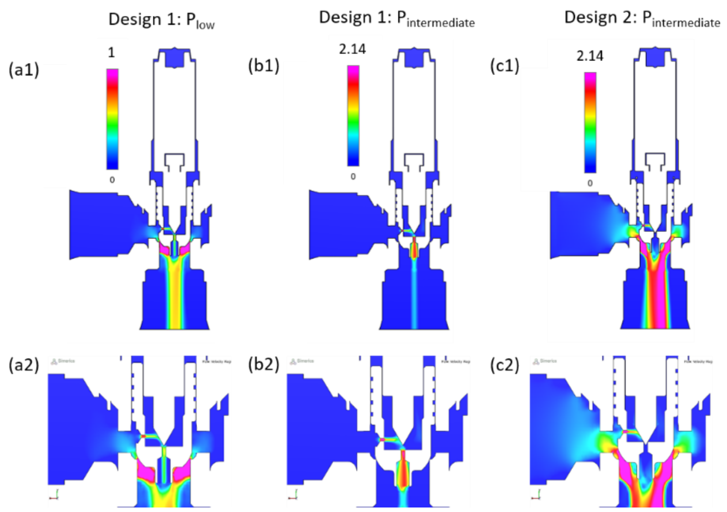

Figure 12: Cross-section showing the velocity contours in the EPF. (a1) Design 1 at inlet pressure P_{low}, where the poppet lifts successfully. (a2) Detailed view of the poppet and pilot lift region for Design 1 at P_{low}. (b1) Design 1 at inlet pressure $P_{intermediate}$, where the poppet fails to lift. (b2) Detailed view of the poppet and pilot lift region for Design 1 at $P_{intermediate}$. (c1) Design 2 at inlet pressure $P_{intermediate}$, where the poppet lifts successfully. (c2) Detailed view of the poppet and pilot lift region for Design 2 at $P_{intermediate}$

Figure 13 shows regions where the total gas volume fraction exceeds 0.1, capturing the combined contribution of vapor, dissolved gas, and free non-condensable gas. Cavitation bubbles form primarily as the poppet begins to lift and extend into outlet port 1. Figure 13a shows Design 1 at an inlet pressure of P_{low} and in Figure 13b, the inlet pressure is at $P_{intermediate}$ for the same design. As the poppet does not lift at this pressure, cavitation is confined to the poppet orifices through which flow leaks. Figure 13c shows Design 2 at $P_{intermediate}$, where the larger gas volume fraction compared to the P_{low} case is consistent with the higher operating pressure and jet velocity.

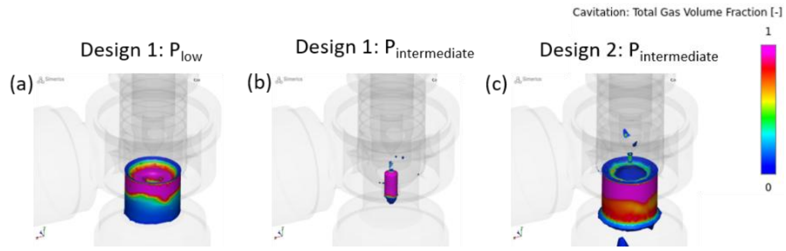

Figure 13: Regions where total gas volume fraction > 0.1 in the EPF. (a) Design 1 at inlet pressure P_{low}, where the poppet lifts successfully. (b) Design 1 at inlet pressure $P_{intermediate}$, where the poppet fails to lift. (c) Design 2 at inlet pressure $P_{intermediate}$, where the poppet lifts successfully.

3D CFD results are validated with test data. The test data in Design 1 in Figure 14a shows a clear increase in flow rate with solenoid current at P_{low}, while the $P_{intermediate}$ case produces less than 0.1 unit flow rate, signaling flow through the poppet orifices only. CFD results, plotted against armature displacement on the same axes, follow the same trends for both pressure conditions, confirming that the simulation correctly captures the poppet's failure to lift at elevated pressure. Figure 14b shows the corresponding data for Design 2 at P_{high}. Both test and simulation demonstrate that the design modification enables full poppet lift at high operating pressures.

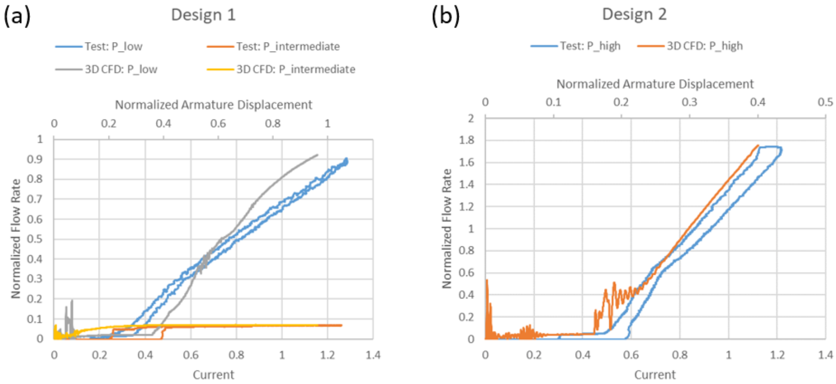

Figure 14: Validation against test data. (a) Test data showing flow rate versus current and CFD data showing flow rate versus armature displacement for Design 1. Poppet fails to lift at an inlet pressure of $P_{intermediate}$, which was also observed in the CFD simulation. (b) Test data showing flow rate versus current and CFD data showing flow rate versus armature displacement for Design 2. Both test and simulation show that the poppet in the new design, Design 2, can lift even at a high inlet pressure of P_{high}.

The validated CFD results provided the confidence to manufacture a prototype, which was subsequently tested successfully. Informed by the CFD pressure analysis across the separate zones, the 1D model was revisited to assign greater significance to the less predictable frictional and viscosity related parameters that had previously been under-constrained. With these adjustments, the 1D model was able to replicate the observed failure behavior successfully across a range of inlet pressures from P_{low} up to P_{high}.

6. SUMMARY

This study presents a decoupled co-simulation methodology for analyzing transient flow behavior and instabilities in hydraulic valves, combining one-dimensional (1D) system modeling with high-fidelity three-dimensional (3D) Computational Fluid Dynamics (CFD) simulations in Simerics-MP+. The methodology was demonstrated on two valves developed by Parker-Hannifin: a poppet-style Logic Element (PLE) and an Electro-Proportional Flow (EPF) control valve. In the decoupled framework, 1D models characterize normal operating conditions and establish model parameters iteratively, while 3D CFD is used to investigate worst-case scenarios and failure modes that cannot be resolved at the system level. For the PLE, CFD reproduced experimentally observed poppet oscillations at low flow rates and enabled rapid computational screening of design variants prior to physical prototyping. For the EPF, CFD identified a pressure-dependent failure mode that 1D modeling could not replicate, leading to a targeted design modification that was validated in simulation and confirmed through physical testing across a range of inlet pressures. Together, these results demonstrate that the decoupled 1D–3D methodology reduces prototyping cycles and accelerates valve development by providing physical insight that is difficult to obtain through 1D analysis or experimental measurements alone. The approach is computationally efficient, preserves realistic system behavior, and is directly applicable to the resolution of complex dynamic issues in modern hydraulic valve designs.

7. REFERENCES

[1] Valdés, J. R., Rodríguez, J. M., Monge, R., Peña, J. C., & Pütz, T. (2014). Numerical simulation and experimental validation of the cavitating flow through a ball check valve. *Energy Conversion and Management*, *78*, 776–786.

[2] Yang, Q., Zhang, Z., Liu, M., & Hu, J. (2011). Numerical simulation of fluid flow inside the valve. *Procedia Engineering*, *23*, 543–550.

[3] Wu, D., Li, S., & Wu, P. (2015). CFD simulation of flow-pressure characteristics of a pressure control valve for automotive fuel supply system. *Energy Conversion and Management*, 101, 658–665.

[4] Lisowski, E., & Rajda, J. (2013). CFD analysis of pressure loss during flow by hydraulic directional control valve constructed from logic valves. *Energy Conversion and Management*, 65, 285–291.

[5] Herakovič, N., Duhovnik, J., & Šimic, M. (2015). CFD simulation of flow force reduction in hydraulic valves. *Tehnicki Vjesnik - Technical Gazette*, 22(2), 453–463.

[6] Taghizadeh, S., Oravec, J., & Dhar, S. (2025). Noise Mitigation Analysis in Relief Valves Using a Hybrid CFD-Acoustics Approach. *Proceedings of the ASME 2025 International Mechanical Engineering Congress and Exposition*.

[7] Gasche, J. L., Demétrio, A., De, S., Dias, L., Domingues Bueno, D., Ferreira Lacerda, J., Gasche, J. L., Dias, A. D. S. L., Bueno, D. D., & Lacerda, J. F. (2016). Numerical Simulation of a Suction Valve: Comparison between a 3D Complete Model and a 1D Model. *International Compressor Engineering Conference.* Paper 2461.

[8] Dhar, S., Ding, H., Lacerda, J., & Lacerda, J. (2016). A 3-D Transient CFD Model of a Reciprocating Piston Compressor with Dynamic Port Flip Valves. *International Compressor Engineering Conference*. Paper 2471.

[9] Chaudhari, N., Ding, H., Gao, H., & Mohapatra, C. K. (2024). Dynamic Reed Valve in Rolling Piston Compressor: A 3-Dimensional Transient CFD Simulation 3-Dimensional Transient CFD Simulation. *International Compressor Engineering Conference.*

[10] Wang, C., Nilsson, H., Yang, J., & Petit, O. (2017). 1D–3D coupling for hydraulic system transient simulations. *Computer Physics Communications*, *210*, 1–9.

[11] Zhang, P., Cheng, Y., Xue, S., Hu, Z., Tang, M., & Chen, X. (2023). 1D-3D coupled simulation method of hydraulic transients in ultra-long hydraulic systems based on OpenFOAM. *Engineering Applications of Computational Fluid Mechanics*, *17*(1).

[12] Schmid, J., Bussard, C., Nicolet, C., Forest, S., Stojanovic-Roth, S., & Saugy, J. N. (2025). Investigation of Pressure Relief Valve Performance from 1D Hydraulic

Transient Model Calibration to Advanced CFD Analysis. *IOP Conference Series: Earth and Environmental Science*, *1561*(1), 012033.

[13] Ding, H., Visser, F. C., Jiang, Y., & Furmanczyk, M. (2011). Demonstration and validation of a 3D CFD simulation tool predicting pump performance and cavitation for industrial applications. *Journal of Fluids Engineering, Transactions of the ASME*, *133*(1).

[14] Singhal, A. K., Athavale, M. M., Li, H., & Jiang, Y. (2002). Mathematical basis and validation of the full cavitation model. *Journal of Fluids Engineering, Transactions of the ASME*, *124*(3), 617–624.